

Dynamic optical chirality based on liquid-crystal-embedded nano-cilia photonic structures

Received: 23 June 2024

Accepted: 6 July 2025

Published online: 17 July 2025



Sufan Li^{1,5}, Yiheng Zhang^{2,5}, Yang Wang¹✉, Guiyuan Cao^{3,4}, Qinghua Liang¹, Xiaochen Zhang¹, Haozhe Sun¹, Yongyue Zhang¹, Zhiyu Wang¹, Xing Liu¹, Peng Chen^{1,2}✉, Han Lin^{3,4}✉, Baohua Jia^{3,4}, Yan-Qing Lu² & Jiafang Li¹✉

Compared to natural chiral molecules, artificial chiral photonic structures offer stronger chiroptical responses. However, the remarkable optical properties of most chiral structures are fixed upon fabrication, limiting their applications in scenarios where a dynamic response is required. Here, we propose an active optical chirality strategy by nano-kirigami and self-organization method, based on which a dual chiral framework is fabricated with cilia structures and cholesteric liquid crystal (LC). This dual chiral framework allows for a dynamic and wide range of chiroptical responses with nanoscale pixel size, enabling amplification, elimination, and reversal of circular dichroism. Furthermore, a thermally tunable chiroptical metalens based on this cilia-LC framework is constructed to achieve a focusing switch of circularly polarized light. This proposed technique holds great potential in diverse fields, including dynamic imaging, optical encryption, tunable displays, and sensors.

Chiral micro/nanostructures or molecules are generally known for their ability to display chiroptical response^{1,2}. One typical feature is circular dichroism (CD), which refers to the difference in response between left and right circularly polarized light (CPL). In the past decade, scientists have developed a variety of chiral metamaterials and verified their application capabilities in many fields^{3,4}, including biochemical sensing⁴, chiral holographic imaging⁵, chiral information encryption⁶, etc. The successful implementation of these applications benefits from the advancement of nanofabrication technology, as strong chiroptical responses generally require complex three-dimensional (3D) nanostructures.

Nano-kirigami⁷, one of the emerging nanofabrication technologies, creates fine two-dimensional (2D) planar curved patterns on thin metal film and transforms them into 3D twisted structures, thereby achieving giant CD^{8–11}. Meanwhile, the deformable characteristics of nano-kirigami metasurface enable dynamic regulation of the amplitude and phase of light¹², presenting a promising approach towards light manipulation in displays and radar systems^{13,14}. However, the spatial deformation of nano-kirigami structures is inherently limited by the geometric shape, making it challenging to achieve a large-range and reversal adjustment of chiroptical response.

Integrating active optical materials onto the metasurface can introduce new regulatory dimensions, offering a potential solution to

¹State Key Laboratory of Chips and Systems for Advanced Light Field Display, School of Physics, Beijing Institute of Technology, Beijing 100081, China.

²National Laboratory of Solid State Microstructures, College of Engineering and Applied Sciences, Collaborative Innovation Center of Advanced Microstructures, Nanjing University, Nanjing 210093, China. ³Centre for Atomaterials and Nanomanufacturing, School of Science, RMIT University, 124 La Trobe Street, Melbourne, Victoria 3000, Australia. ⁴The Australian Research Council (ARC) Industrial Transformation Training Centre in Surface Engineering for Advanced Materials (SEAM), RMIT University, 124 La Trobe Street, Melbourne, Victoria 3000, Australia. ⁵These authors contributed equally: Sufan Li, Yiheng Zhang. ✉e-mail: yangwang@bit.edu.cn; chenpeng@nju.edu.cn; han.lin2@rmit.edu.au; jiafangli@bit.edu.cn

this challenge^{15–17}. Among numerous functional materials, liquid crystals have been widely applied in display, holographic imaging, tunable laser, etc^{18–25}. In particular, the cholesteric liquid crystal (LC) molecular units self-assemble into an elegant spiral structure and form the one-dimensional chiral photonic crystal, resulting in Bragg reflection with strong circular polarization selectivity^{26,27} (i.e. CPL photonic bandgap). Under the stimulation of external physical fields^{28,29}, the LC helices reorganize, which can cause the shift of the CPL photonic bandgap and the quasi-continuous modulation of the transmission at the bandgap edge^{30,31}. Nevertheless, for traditional cholesteric LC materials, their chiroptical response chirality is generally hard to reverse, and structured LC devices are limited to a fabrication resolution typically at the micrometer scale, resulting in a relatively large pixel size.

The above two examples articulate the geometric and structural limitations of current artificial chiral structures. Nowadays, many modern optical systems require dynamic and high-performance light modulation. In order to achieve chiroptical manipulation with large modulation range and high resolution, it is necessary to explore a solution that can break these limitations.

In this work, we propose a dual chiral framework by integrating nano-cilia structure and cholesteric LC units, which achieves dynamic and continuous circular dichroism amplification and reversal. These delicate chiral structures with a strong chiroptical response and circular polarization photonic bandgap in visible region are fabricated by efficient nano-kirigami and self-assembly method. The proposed framework breaks the physical limit of conventional nano-kirigami structures, and offers tuning capability beyond the resolution of cholesteric LC. On this basis, we demonstrated a thermally tunable metalens that enables a dynamic focusing switch of CPL. The structural designs, preparation methods, and application demonstration make this dual chiral framework a promising platform for future research in optical communication, display, sensor, etc.

Results

Design of the dual chiral framework for dynamic circular dichroism modulation

Generally, 3D structures with twisting features in the propagation direction such as helices are highly desirable to realize strong optical chirality. As shown in the Fig. 1a, a left-handed helix can be stretched and compressed to change the chiroptical response of the structure. However, if one wants to completely reverse the structure from left-handed to right-handed, the system needs to overcome a giant energy barrier. Here, we propose a universal strategy to fully address this problem, namely the dual chiral framework. Its basic principle is to achieve continuous modulation of CD response through the constructive and destructive effects of two chiral structures (Fig. 1b). The chirality of helical structures can be described by helicity (H)³²:

$$H = \frac{1}{n} \sum_{i=1}^n \phi_i d_i, \quad (1)$$

where n is the number of chiral units, ϕ_i is the torsion angle of the structure, d_i is the distance along the spiral axis. For the simplest case, which is a structure composed of two chiral units, its helicity (H_2) can be expressed as:

$$H_2 = \frac{1}{2}(\phi_1 d_1 + \phi_2 d_2). \quad (2)$$

When the torsion angle is greater than zero, the structure can be considered right-handed, otherwise it is left-handed. Therefore, the key to achieve chiroptical reversal can be represented by the following

equation:

$$\phi_1 d_1 + \phi_2 d_2 = 0, \quad (3)$$

which means finding the zero chiral point of the framework. Equation 3 demonstrates the connection between two units. However, the above equations do not provide a direct answer for high-precision in-situ chiroptical reversal. We have solved this problem through a design that combines stationary and dynamic helical structures. Specifically, we first design a stationary nano-cilia structure to determine the operating wavelength and bandwidth of the overall framework, and then combine it with scalable liquid crystal helix to achieve chiroptical reversal and states control.

The schematic of the cholesteric liquid-crystal embedded nano-cilia photonic structure is shown in Fig. 1c. The incident CPL interacts with the cholesteric LC and the nano-cilia successively. Both structures have different transmittance for right- and left-handed CPL, thus forming a dual chiroptical response. Functionally, the nano-cilia structure provides a giant static CD value, and the LC layer provides tunability to the framework. Here, CD is defined as

$$CD = (T_{RCP} - T_{LCP}) / (T_{RCP} + T_{LCP}), \quad (4)$$

where T_{RCP} and T_{LCP} denotes transmittance of right- and left-handed CPL respectively. The framework shown in the Fig. 1c is composed of right-handed nano-cilia (RH-cilia) and right-handed LC (RH-LC). At low temperatures, the chiroptical response of the framework is mainly determined by RH-cilia, resulting in a positive CD. At a certain high temperature, RH-LC shows strong modulation effect on RCP light, and the combined chiroptical response causes the reversal of CD.

To achieve chiroptical regulation, the response wavelength of these two elements should match with each other. The optical response range of liquid crystals are generally within the visible wavelengths, while constructing chiral nano-kirigami structures in this range becomes a critical challenge as the 3D deformation ability of the structure weakens as the size of the structure decreases. A main reason is that former closed-loop designs^{33–35} typically result in interference between adjacent elements, making it challenging to downsize the nano-kirigami structures. To address this problem, we adopted a nano-cilia design³⁶, an open-loop structure that enabled us to achieve a nanoscale kirigami structure with optical responses in the visible wavelengths.

The nano-cilia metasurface is constructed on a gold/quartz substrate. Figure 1d shows the electric field distributions of RH-cilia. The cantilever of cilia structure spirals in the direction of light propagation, thus having a modulation effect on CPL. The RH-cilia exhibits stronger plasmonic resonance to LCP, resulting in lower transmittance of LCP compared to RCP. Therefore, according to the definition of CD, RH-cilia shows a positive CD value and LH-cilia shows a negative CD value. The cholesteric LC was then bonded on the back of the quartz substrate. The helical organization of LC molecules causes a chiral photonic bandgap centered at $\lambda_{\text{center}} = n_{\text{ave}} P$, where n_{ave} is the average refractive index of the cholesteric LC, and P is the helical pitch. The CPL component with the same handedness as that of the chiral LC structure will be sufficiently reflected within the bandgap, while the opposite CPL will transmit for all wavelengths³⁷. For a certain wavelength, the dynamic modulation in CPL transmission could be obtained by a tunable pitch P . Figure 1e qualitatively depicts the variation of T_{LCP} and T_{RCP} as a function of the temperature in the RH cholesteric LC. A higher temperature leads to a shorter pitch, thus a blueshift of the bandgap. As a result, T_{RCP} decreases to nearly zero (ON state) and then increases back to nearly 100% (OFF state) during heating, while T_{LCP} is unaffected. In such a case, the CD value of the RH-LC approaches zero (OFF state) or takes a negative maximum (ON state) when the incident wavelength is outside or within the bandgap, correspondingly. In

contrast, an LH-LC exhibits a tunable CD value from nearly zero to a positive extreme.

The CD response of the framework is manifested as the transmission difference between LCP and RCP. In our framework designs,

nano-cilia and LC with opposite chiroptical response (+CD and -CD) enables the elimination or reversal of CD, while nano-cilia and LC with both positive chiroptical response (+CD and +CD) can achieve amplification of CD. Figure 1f, g show two implementation examples of the

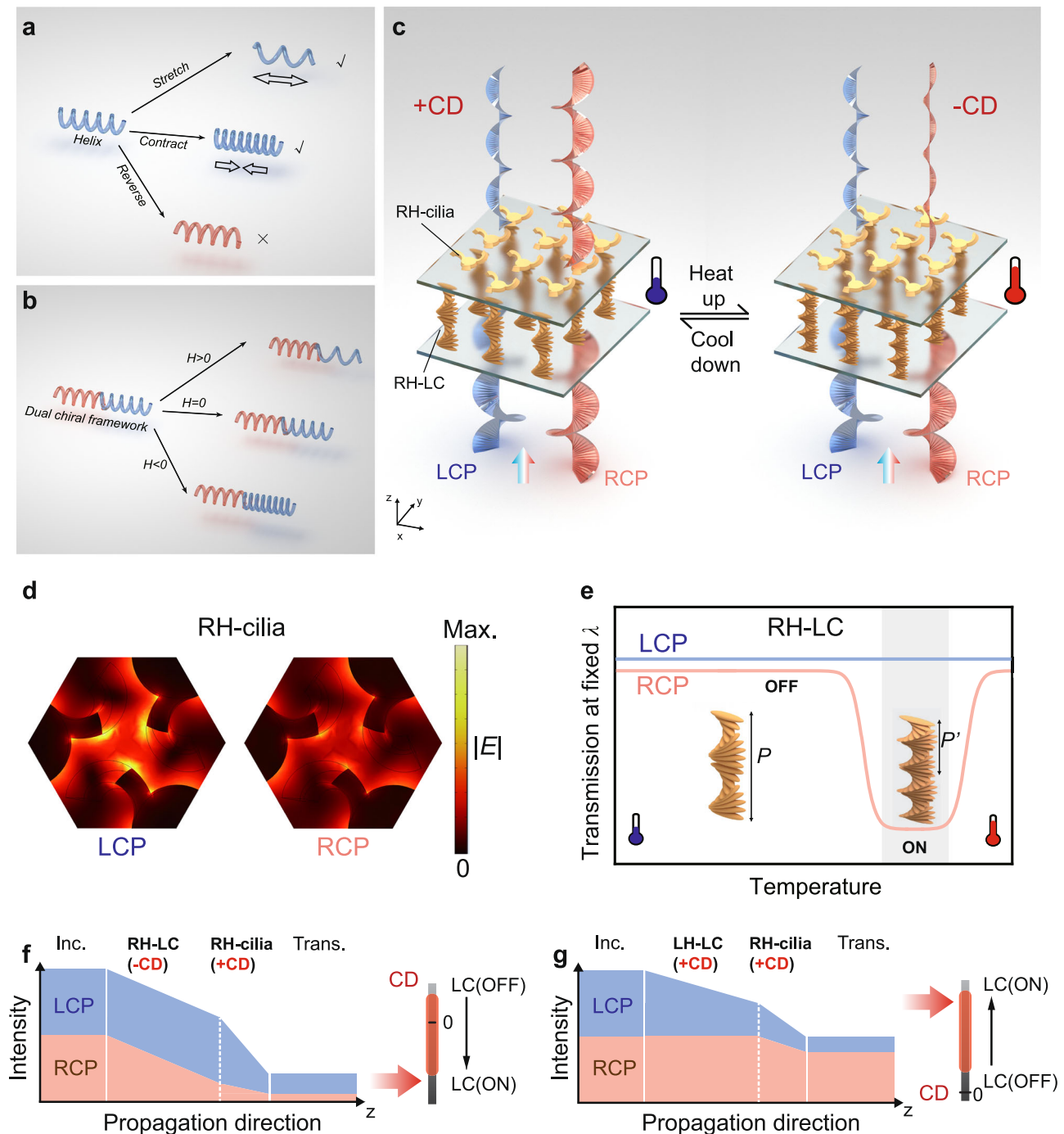


Fig. 1 | Design of dual chiral framework. **a, b** Functional design for dynamic optical chirality. A helix structure (**a**) can be stretched and contracted to alter its chiroptical response. If one wants to completely reverse the structure from left-handed (LH) to right-handed (RH), the system needs to overcome a giant energy barrier. For a dual chiral framework (**b**), dynamic modulation between positive and negative values can be achieved by matching the zero points of their helicity (H). **c** Schematic of the framework made by nano-cilia metasurface integrated with thermoresponsive cholesteric liquid crystal (LC). The dual chiral structures enable the amplification, elimination, and reversal of chiroptical response at different temperatures. **d** Electric field distributions of RH-cilia. The RH-cilia exhibits stronger plasmonic resonance to LCP, resulting in lower transmittance of LCP compared

to RCP. **e** Schematic of the chiral transmission of LC versus temperature at fixed wavelength (λ). The thermoresponsive LC pitch (P) will shrink after being heated, leading to a blueshift of the CPL photonic bandgap and the subsequent change in transmission. When the bandgap shifts, the transmission initially decreases, reaches and maintains a minimum, and finally increases. The gray background marks the “ON” state of the LC. **f, g** Illustration of different combinations of two chiral elements to obtain a tunable and dual chiral framework. In (**f**) the nano-cilia and LC with opposite chiroptical response (+CD and -CD) enables the elimination and reversal of CD. In comparison, in (**g**) nano-cilia and LC with both positive chiroptical response (+CD and +CD) can achieve the amplification of CD.

dual chiral framework. For the RH-cilia with +CD, by combining the right-handed LC (RH-LC) with tunable -CD (Fig. 1f), the T_{RCP} decreases from higher than T_{LCP} to lower than T_{LCP} . Specifically, the incident CPL interacts with the cholesteric LC and the nano-cilia successively. RH-LC only has the ability to modulate T_{RCP} , while RH-cilia has a positive CD response itself. When RCP light passes through the RH-LC, the light intensity decreased (or maintained) when LC is on (or off), while the LCP light intensity does not change. Therefore, when the RCP transmittance of RH-LC approaches 100% at the off state, there is no modulation effect on T_{RCP} in the RH-LC region and the framework maintains a totally positive CD response due to the RH-cilia. In comparison, when the RCP transmittance of RH-LC approaches 0% at the on state, T_{RCP} is less than T_{LCP} in the RH-LC region, thus achieving a negative CD in the RH-LC region. In such a case, the overall CD value after passing through the nano-cilia could be negative, zero, or positive, dependent on the situation of LC.

As for the combination of RH-cilia and LH-LC (Fig. 1g), the T_{LCP} decreases in the LCP photonic bandgap, while T_{RCP} remains the same. Therefore, the difference of T_{LCP} and T_{RCP} enlarges, amplifying the positive CD response.

Fabrication and spectral performance of the chiral nano-cilia metasurface

The detailed fabrication process of nano-cilia is shown in Fig. 2a. The two-dimensional (2D) nano-cilia pattern is directly formed by high-dose focused ion beam (FIB) milling. After that, wet-etching process is applied by HF solution (HF: H₂O = 1:4) for 45 s. The HF solution etches beneath SiO₂ through Au slits, and the arms of nano-cilia are released from the substrate. Then, low-dose global ion beam (GIB) irradiation is employed to induce tensile stress for final deformation, transforming the originally 2D planar nanostructure to 3D twisted nano-cilia structure. To create a chiroptical response in visible wavelengths, the nano-cilia structures are designed with a periodicity of $p = 500$ nm, a central cylinder radius with $r = 130$ nm, and an arm width of $w = 60$ nm (Fig. 2b). Three suspended arms of nano-cilia are initially planar (Fig. 2c) and then deformed by introducing inner stress through GIB irradiation³⁸ (Fig. 2d). These twisted structures provide a physical basis for chiroptical response.

Quantitatively, the ion beam irradiation can be described by the dosage of ion beam. For FIB milling, a high dosage of >50 pC/ μm^2 is employed to cut the 2D nano-patterns. Then, the deformation of the nano-cilia is realized by globally irradiating the entire metasurface with a relative low dose of $0.1\text{--}5$ pC/ μm^2 . The main mechanism of the nano-deformation is to use the residual stress induced by the gallium ion collisions with the gold thin films. Figure 2e shows the deformation height of the nano-cilia as a function of the ion dose. When the gold nanofilm is irradiated by ion beams, some gold atoms are knocked out, causing surrounding atoms to aggregate towards the vacancies, resulting in tensile stress close to the surface of the film. Meanwhile, the inner atoms are subjected to compressive stress due to the influence of implanted gallium ions. These two types of stresses occur within a thickness of ~ 20 nm on the top layer of the gold film⁸, which further drives the elastic deformation of bottom layer. In such a case, the residual stress will cause the structure to bend globally under the guidance of the initial topographies until new equilibrium morphologies are reached (Fig. 2f).

Figure 2g shows simulated CD spectra of 3D deformed RH- and LH-cilia. Due to the vertical deformation of three metallic nano-cilia arms, the mirror symmetry was broken and a resonance peak appears at 690 nm (see detailed analysis in Supplementary Information Note S1). The transmissions of LCP and RCP show great difference, which causes a narrow CD peak at this wavelength. The resonance peak and intensity are mainly decided by the handedness-dependent excitation of electric dipole mode at the tip of the nano-cilia (see detailed analysis in Supplementary Information Note S2). Figure 2h, i present

the experimental transmission and CD spectra of 3D deformed RH- and LH-cilia, with a maximum CD of 0.46 at 690 nm. These results well match with theoretical simulations in terms of resonance wavelength, while the differences in resonance intensity and linewidth are mainly due to structural deviations during the fabrication process. The implantation of Ga⁺ ions during FIB milling and irradiation introduced optical loss, which broadened the resonance peak of nano-cilia. Meanwhile, incomplete wet etching process resulted in residual SiO₂. The capillary forces during the drying process of the wet etching may lead to the imperfect deformation of some of the suspended nano-cilia arms. Nevertheless, the structure remains stable once fabricated. The deformation of nano Au arms under ion induced stress does not change with temperature (see spectral stability of nano-cilia metasurface in Supplementary Information Note S3).

The deformation mechanism of nano-cilia is to utilize the residual stress generated by the collision between ions and gold films, which creates a stress difference between the surface and inner layer of the gold film, leading to the structural distortion. This deformation trend is unidirectional, therefore reversible optical modulation and CD reversal cannot be achieved. To address this issue, we introduced another chiral material to participate in CPL modulation, namely cholesteric LC.

Optical properties of cholesteric liquid crystal

The preparation of cholesteric LC was achieved by mixing the thermoresponsive RH/LH chiral dopants R811/S811 with nematic liquid crystal E7 (Fig. 3a) at a carefully designed ratio³⁹. After injected into a cell, the LC molecules assemble to uniform standing helices with a pitch length P and parallel directors at both surfaces (Methods). Due to P determining the wavelength of photonic bandgap, thicker LC has more pitches with the same photonic bandgap (Fig. 3b). The helical pitch becomes shorter in response to heat stimulation, and the resultant bandgap blueshifts. As a result, the cholesteric LC texture appears dark gray at 24 °C and red at 34 °C (Fig. 3c), since their reflection are within the infrared and red range, respectively.

The surface anchoring of the cell restricts the LC pitches to the discrete set $P = D/N$, where D is the cell gap (i.e., sample thickness) and the pitch number N must be an integer or a half integer. Therefore, the photonic bandgap is tuned quasi-continuously (Fig. 3d), and the cell of $D = 7.5$ μm allows more stable intermediate states and smaller intervals than that of $D = 4.0$ μm (see detailed analysis in Supplementary Information Note S4). The in-situ transmission spectra of the thermoresponsive cholesteric LCs with different D are shown in Fig. 3e, f. Due to the larger pitch number, the transmission bandgap edge of thicker samples is steeper. The bandgaps demonstrate a distinct blueshift with increasing temperature (Fig. 3d). Figure 3g illustrates the detailed process of transmission recovering at 690 nm as the bandgap shifts away. In the cell of $D = 7.5$ μm , since the heat-driven regulation in the pitch could take smaller intervals, T_{LCP} changes in a smoother way, instead of a drastic change (see detailed analysis of dynamic response in Supplementary Information Note S5). Notably, the LC cell gap provides a way to adjust the thermal sensitivity of the dual chiral framework.

Dynamic CD modulation enabled by the dual chiral framework

We integrate cholesteric LC onto the back of the quartz substrate loaded with nano-cilia to form the dual chiral framework. A homemade optical characterization setup was employed to measure the dynamic CD modulation capability of the sample (Fig. 4a). A halogen light served as the light source, emitting a light beam that illuminated the fabricated sample. The light beam passed through a linear polarizer (LP) and a quarter-wave plate (QWP) to generate CPL. Subsequently, the light beam was focused on the sample by using a $20\times$ objective lens. The sample was placed on a heating stage and the CD modulation process was recorded by a spectrometer.

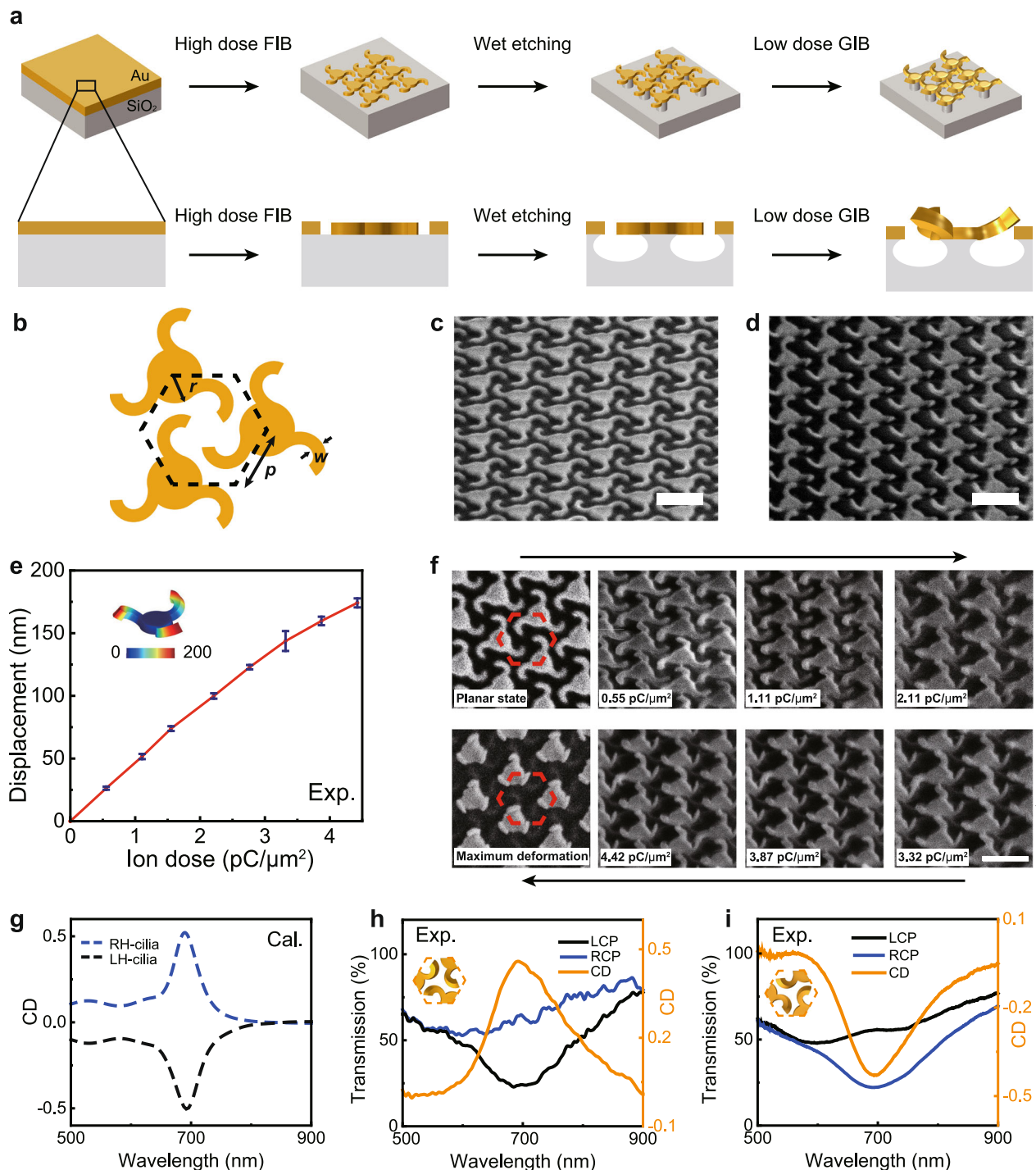


Fig. 2 | Fabrication and chiroptical response of nano-cilia structures. **a** The preparation process of nano-cilia metasurface. The nano-cilia structure is realized by a nano-kirigami process: a high dose focused ion beam (FIB) is used for film cutting, and then a low dose global ion beam (GIB) is used for structure twisting. **b** Schematic of nano-cilia units. The units are designed with a periodicity of $p = 500$ nm, a central cylinder radius with $r = 130$ nm, and an arm width of $w = 60$ nm. **c**, **d** Side-view SEM images of 2D and 3D state of nano-cilia metasurface.

Scale bars: 500 nm. **e** Experimental vertical displacement of the nano-cilia as a function of ion dose. Error bars represent standard deviation (SD) of three independent experiments ($n = 3$). **f** SEM images of nano-cilia metasurface with different displacement. Scale bar: 500 nm. The initial and final images are top views, and the intermediate images are oblique views with an angle of 52° . **g** Calculated CD spectra of 3D deformed RH/LH-cilia. **h**, **i** Experimental transmission and CD spectra of 3D deformed RH/LH-cilia under LCP and RCP excitation.

The static CD spectra of dual chiral frameworks based on RH-cilia are shown in Fig. 4b. For a framework with LH-LC, T_{LCP} decreases due to the Bragg reflection. Therefore, the difference between the original high T_{RCP} and the low T_{LCP} of nano-cilia structure is further enlarged (see optical transmission spectrum in Supplementary Information Note S6), leading to a CD enhancement from 0.46 to 0.84. Conversely,

for a framework with the RH-LC, T_{RCP} decreases from a value higher than T_{LCP} to a value lower than T_{LCP} . So, the initial positive CD will be modulated from 0.46 to a negative CD of -0.76 . LCs have the ability to reduce the transmittance of one CPL from its initial value to nearly 0. In such a case, the transmitted RCP and LCP light at the entrance of the RH-cilia are different, resulting in asymmetry between the maximum

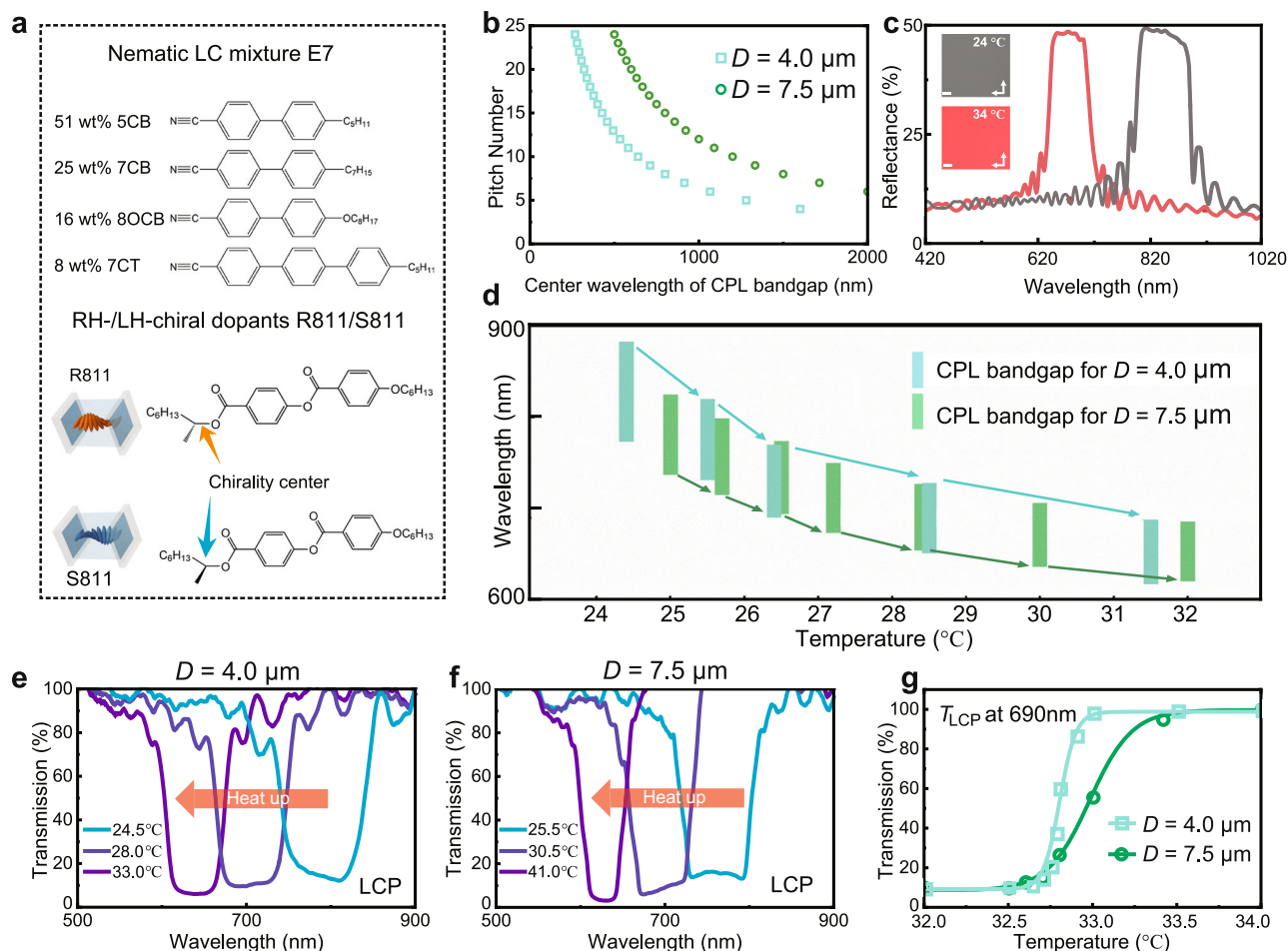


Fig. 3 | Optical properties of cholesteric liquid crystal. **a** Molecular structures of nematic LC mixture E7, and thermoresponsive RH/LH chiral dopant R811/S811. **b** The calculated relation between the cholesteric LC pitch number and the center wavelength of the CPL photonic bandgap. The center wavelength is calculated by $\lambda_{\text{center}} = n_{\text{ave}} P = n_{\text{ave}} D / N$, where n_{ave} is the average of the ordinary and the extraordinary refractive indices of the cholesteric LC, D is the cell gap, P is the pitch, and N is the pitch number expressed by $N = D/P$. **c** Reflection spectra of 7.5 μm LH-LC at 24.0 °C (gray line) and 34.0 °C (red line). Inset: Microscopic reflection images of the 7.5 μm LH-LC at 24.0 °C and 34.0 °C. White arrows denote the polarization of the

crossed polarizers. Scale bars: 100 μm . **d** The shift of bandgaps for the 4.0- μm (cyan) and the 7.5- μm (green) LH-LCs. Each bar denotes a stable state, whose upper and lower boundaries mark the photonic band gap edges, and the horizontal location represents the temperature. **e, f** Transmission spectra of 4.0 μm and 7.5 μm thick LH-LC under LCP excitation at different temperatures. The arrows indicate the blueshift of bandgap when the temperature increases. **g** Dynamic transmission of 4.0 μm and 7.5 μm thick LH-LC under LCP excitation at wavelength of 690 nm.

and minimum CD of the two frameworks. Meanwhile, the changes in RCP or LCP transmittance will simultaneously affect both the numerator and denominator of the CD equation (Eq. 4), resulting in a small difference in absolute CD values between the two frameworks.

The above CD features are the optical response of the frameworks at a fixed temperature, which can be further modulated by heating the cholesteric LC. As is shown in Fig. 4c, we illustrate the dynamic CD modulation process of the dual chiral frameworks in a single wavelength perspective ($\lambda = 690 \text{ nm}$). For the framework with LH-LC (Fig. 4c, blue curve), the blueshift of the CPL photonic bandgap causes the dynamic modulation of the T_{LCP} . The T_{LCP} gradually decreases when the CPL photonic bandgap includes 690 nm, and recovers when the CPL photonic bandgap moves out. Therefore, the CD of the framework is amplified at first and then recovered. Different modulation processes happen to the framework with the RH-LC (Fig. 4c, orange curve). The T_{RCP} is modulated from initially higher than T_{LCP} and finally to lower than T_{LCP} . Three chiroptical response states occur during this process: positive CD, non-chirality, and negative CD. The extremum of CD occurs at difference temperatures for the framework with different chiral LC. This is due to slight differences in the temperature response

of LC with different chiral dopants R811/S811. We measured the transmission of two different cholesteric LCs at 690 nm as a function of temperature (see Supplementary Information Note S7). The results indicate that the cholesteric LCs have different transmission valley, which is consistent with Fig. 4c.

As we have mentioned above, the thickness of LC will affect the sensitivity of CD modulation. We heated the device with a uniform heating rate and recorded the CD at different temperatures in situ (Fig. 4d, e). The framework with a 4.0 μm -thick LC has a faster thermal response, while a 7.5 μm -thick LC gives the slower changing of CD (see detailed analysis in Supplementary Information Note S5). We can choose appropriate device thickness according to the requirement of application scenarios.

Thermally tunable CPL metalens

It can be seen from the above experiments that embedding different types of cholesteric LC on the same nano-cilia metasurface can realize different types of chiroptical regulation. Furthermore, we can also combine different types of nano-cilia on the same LC to achieve light field regulation of CPL. Here, we designed a thermally tunable CPL

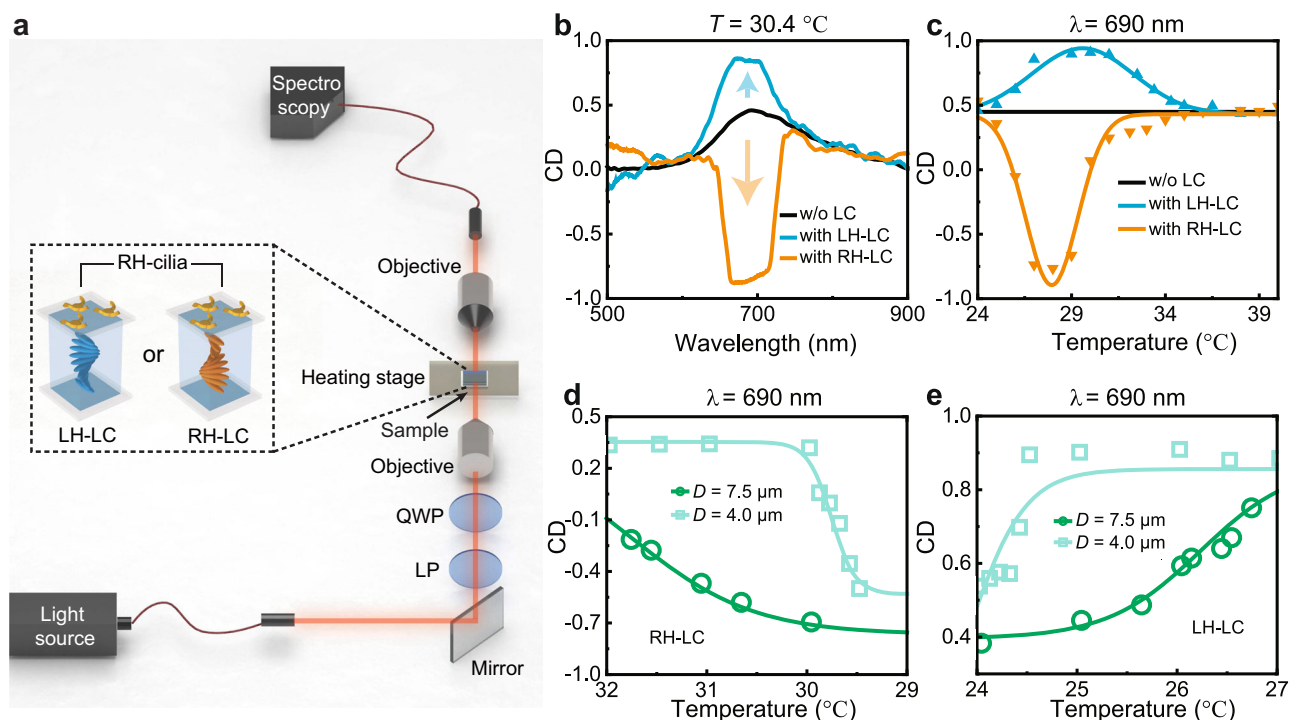


Fig. 4 | Dynamic CD modulation of the dual chiral framework based on RH-cilia. **a** The optical characterization setup. Inset shows the dual chiral framework of RH nano-cilia with LH- or RH-LC. **b** Static CD spectra of frameworks with LH-/RH-LC at temperature of 30.4 °C. **c** Dynamic CD modulation of frameworks with LH-/RH-LC

as a function of temperature. **d, e** Detailed CD modulation process of frameworks with different LC thicknesses. The framework integrated with RH-LC (**d**) demonstrates the process of CD reduction and reversal. The framework integrated with LH-LC (**e**) demonstrates the process of CD amplification.

focusing metalens by utilizing the giant CD modulation ability of the dual chiral framework. Figure 5a depict the schematic of the metalens. Considering a beam of LCP light incident on the structures, RH-cilia has a lower LCP transmittance compared to LH-cilia. By designing a metasurface with a circular transmittance distribution (Fig. 5b, c), chiroptical focusing can be achieved. Furthermore, thermoresponsive cholesteric LC can adjust the intensity of incident LCP, eliminating the circular transmittance distribution, allowing the metalens to switch between focused and non-focused states.

Experimentally, we constructed 37,440 nano-cilia units with an area of $80\ \mu\text{m} \times 80\ \mu\text{m}$, which employs two types of nano-cilia structures to form several concentric rings on LH-LC. Figure 5d shows the SEM image of the first order ring. These nano-cilia units are arranged in a hexagonal pattern, with the RH-cilia forming fine rings and the rest being LH-cilia (Fig. 5e). The width of the rings is only one pixel, and each pixel of the metalens contains only one nano-cilia unit. The position of each ring is determined by using the Rayleigh–Sommerfeld diffraction method^{40–42}. These rings consist of LH- and RH-cilia have different transmittance for incident CPL, which enable the focusing of light. Here, we introduce CD_{lens} to evaluate the optical response of the CPL metalens:

$$CD_{lens} = (T_{LHC} - T_{RHC}) / (T_{LHC} + T_{RHC}), \quad (5)$$

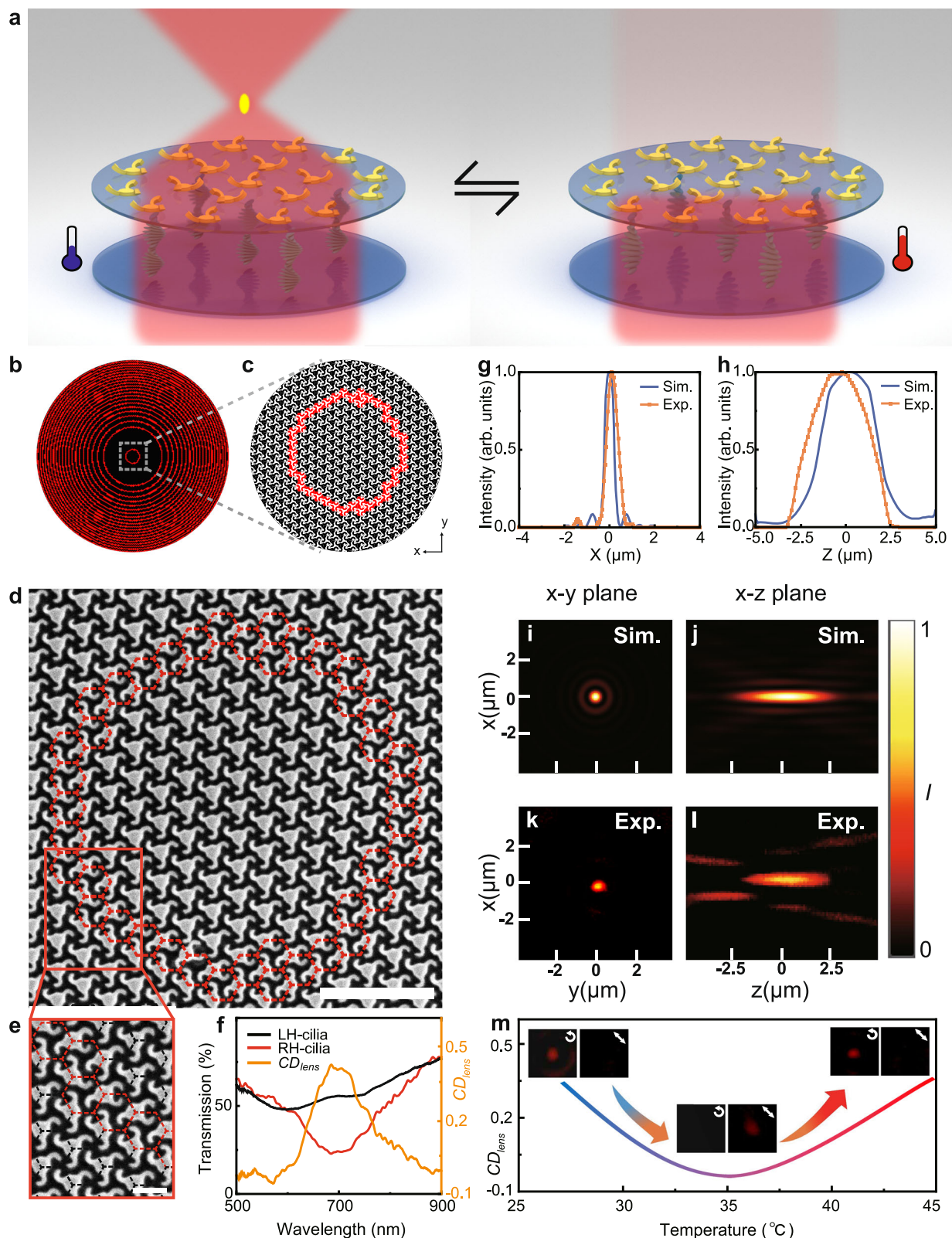
where T_{LHC} and T_{RHC} are the transmittance of LH- and RH-cilia. Figure 5f shows the LCP transmittance of LH- and RH-cilia. The LH-cilia has a transmittance of 55% at 690 nm, while the RH-cilia has a transmittance of only 23%, resulting in a CD_{lens} of 0.41.

Theoretical simulation of the intensity distribution of the designed metalens in the focal region is shown in Fig. 5g, h. The focal length is designed to be $50\ \mu\text{m}$. The metalens is able to achieve sub-wavelength focusing performance in the x-y plane as the full width at half maximum (FWHM) is $450\ \text{nm}$, corresponding to 0.65λ at the incident wavelength of 690 nm. Meanwhile, a high resolution of $3.3\ \mu\text{m}$

(4.7λ) along the z-direction is also achieved. The corresponding experimental demonstration (Fig. 5g, h, orange line) show a high resolution of $582\ \text{nm}$ (0.84λ) and $3.8\ \mu\text{m}$ (5.5λ) in the x-y plane and along the z-direction, respectively.

We compared the simulated and experimental focal point image on x-y and x-z plane (Fig. 5i–l), the well-matched results confirm the high accuracy of the nano-kirigami method. This achievement signifies the successful development of a tunable CPL metalens, demonstrating its adaptability and functionality in response to thermal conditions. Considering the focal length and numerical aperture (NA) of the metalens can be flexibly designed and controlled, and the small size ($80\ \mu\text{m} \times 80\ \mu\text{m}$) allows convenient integration of such a metalens on the facet of an optical fiber that has a typical diameter of $>100\ \mu\text{m}$. Our thermally tunable metalens can be used as an optical modulator to encode 0 and 1 for optical communications. Meanwhile, the high spatial resolution allows the use of our metalens in a fiber optic endoscope to achieve miniaturized size and high-resolution optical imaging for broad applications^{43,44}.

The dynamic modulation process of the CPL metalens is shown in Fig. 5m. For an incident LCP light at the wavelength of 690 nm, the metalens exhibited focusing ability owing to the different transmission of two types of nano-cilia at 25 °C. The center wavelength of the LCP Bragg reflection band shifted to 690 nm when the metalens was heated to 35 °C, and the focusing function was disabled due to the elimination of CD_{lens} . When the temperature reaches 41 °C, the Bragg reflection band blue shifted to a much shorter wavelengths, away from 690 nm, so the metalens regained its focusing ability. As can be seen, this metalens can undergo continuous changes in focused and defocused states within the range of 25 °C to 41 °C. Interestingly, our metalens exhibits a reversed response to linearly and circular polarized light: it focuses incident linearly polarized light when the LC is activated, but not when deactivated (Fig. 5m inset, see Supplementary Information Note S8 for details). Given its imaging capability, this metalens shows potential for multispectral imaging of polarization-sensitive objects.



In the above experiments, we utilized the difference in transmittance between LH- and RH-cilia to achieve different focusing effects for different polarized light. Another interesting combination is to arrange cilia with different rotation angles for geometric phase modulation, which enables circular polarization switching (see Supplementary Information Note S9). In our framework design, the twist of the liquid crystal is responsible for dynamic modulation, while the static cilia structure can

be designed and arranged in multiple dimensions such as the number, length, width, and height of the arms, allowing our device able to not only modulate CD response, but also achieve rich applications.

Discussion

Generally, the optical chirality of materials is determined by their geometric structure and dielectric functions. Although dynamic CD

Fig. 5 | Thermally tunable CPL metalens. **a** Schematic of thermally tunable metalens. **b** Schematic of the metalens design, with the RH-cilia (red) forming the fine ring and the rest being LH-cilia (black). By designing a metasurface with a circular transmittance distribution, chiroptical focusing can be achieved. **c** Illustration of the metalens' first order concentric ring. **d** The SEM image of the metalens' first order concentric ring. RH-cilia structures are framed by red dashed line. Scale bar: 2 μm . **e** Detailed SEM image of the LH- and RH-cilia in the metalens. RH-cilia structures are framed by red dashed line, and LH-cilia structures are framed by black dashed line. Scale bar: 500 nm. **f** Experimental transmission spectrum of

LH- and RH-cilia structures under LCP excitation. Orange line shows the CD_{LH} spectrum. **g** Cross-sectional focal point intensity plots along the x-direction. **h** Cross-sectional focal point intensity plots along the z-direction. **i–l** Simulated and experimental focal point image. **m** Dynamic focusing switch of the metalens. The CD_{LH} first decreases and then increases with temperature, during which the metalens initially loses its CPL focusing ability and then refocuses again. Insets show the optical image of the focal position. The metalens exhibits a reversed response to circular and linearly polarized light.

response can be achieved by adjusting these parameters, the complete reversal of chirality requires overcoming large structural or molecular barriers, which has rarely been reported. Recent works have made significant progress in this area, such as CD redshift in the near-infrared wavelengths based on phase change materials⁴⁵, and asymmetric CD response in chiral microcavities⁴⁶. However, continuous and broadband modulation of dynamic chiral reversal remains elusive (see Supplementary Information Note S10 for more comparisons with existing CD modulation methods). To tackle these challenges, we propose the concept of dual chirality in this work. Meanwhile, by using the nano-kirigami technology, we have realized the wavelength matching between the metasurface and the LC molecules, thus achieved high-resolution CD modulation.

In conclusion, we have proposed and demonstrated a dynamic chiroptical platform via liquid-crystal-embedded nano-cilia photonic structures. Through nano-kirigami method, we prepared open-loop nano-cilia structure with a giant chiroptical response in visible region. A thermoresponsive cholesteric LC with dynamic CPL photonic bandgap is well integrated to the nano-cilia metasurface. This dual chiral framework can dynamically amplify, eliminate, and reverse the CD response. Precise temperature control allows a selective range of the CD value from -0.76 to 0.84 . Moreover, a thermally tunable and compact CPL metalens is demonstrated which can be dynamically switched between focusing and defocusing state. This integrated device with dynamic CD has great potential in optical communication, displays, sensors, etc.

Methods

Preparation of nano-cilia metasurface

The 2D nano-cilia structures were fabricated with a dual-beam FIB/SEM system (FEI Helios 600i) on a metal/SiO₂ substrate. The kirigami pattern was built on the commercial Au/SiO₂ substrates (60 nm Au, 2 μm SiO₂). The 2D patterns were directly cut by the FIB under high doses of (>50 pC/ μm^2). The acceleration voltage and current beam of Ga⁺ were set at 20 kV and 40 pA, respectively. After the cutting processes, the sample was dipped into diluted hydrofluoric acid (20%, HF:H₂O = 1:4) to etch off the beneath SiO₂, resulting in locally suspended kirigami patterns on the top. Wet etching is an isotropic etching process with an etching rate of 55 nm/min. Consequently, selecting 45 s for etching results in the removal of 41.25 nm of SiO₂, which is sufficient to etch away the SiO₂ beneath the nano-cilia arm (width: 60 nm) while leaving the SiO₂ cylinder with a sufficient diameter of ~ 200 nm beneath the central disk to support the structure. Then, the 2D structures were irradiated by ion beam irradiation with relative low doses of 0.1–5 pC/ μm^2 , deforming to 3D structure.

Preparation of thermoresponsive cholesteric LC

The thermoresponsive cholesteric LC materials were fabricated by mixing the nematic LC host E7 (HCCH, China) with the left-handed/right-handed chiral dopant S811/R811 (HCCH, China). Specifically, the right-handed LC was prepared by mixing the nematic LC E7 with the RH chiral dopant R811, and the left-handed LC was prepared by mixing E7 with the LH dopant S811. Each LC was independently prepared to ensure clear handedness. The doping concentration was 23.24 wt%. To prepare the cholesteric LC device, two pieces of glass substrates were

separated using spacers and sealed with epoxy glue to form a cell. Two types of cell gaps were used, namely 4.0 μm and 7.5 μm , which were checked by the Fabry–Pérot interference. All cells underwent the uniform and anti-parallel alignment with a very small pretilt angle. The cholesteric LC material was filled into the cell at 80 °C, and gradually cooled to room temperature to achieve a uniformly self-assembled LC chiral structure.

Optical characterizations

The optical measurements in the visible wavelength range were performed using a home-made spectroscopy system designed to characterize samples with small sizes. For transmission spectral measurement, a halogen light source (HL-2000, Ocean Optics) served as the light source, the light beam passed through a linear polarizer (GLC-051002, Daheng Optics) and a quarter-wave plate (GCL-060802, Daheng Optics) to convert the input beam polarization into circular polarization state. Subsequently, the light beam was focused on the sample. Finally, the transmitted light in normal direction was collected by the objective lens ($\times 20$, NA 0.25, Olympus) and delivered to a spectrometer (Ocean Optics, QE65000 for visible wavelengths). The optical measurements of the metalens were performed using the home-made spectroscopy system integrated with a piezoelectric ceramic displacement platform. By gradually adjusting the distance between the objective and the metalens in a step of 100 nm, we are able to obtain the optical intensity distributions at different axial positions.

Data availability

All data supporting this study and its findings are available within this published article and its supplementary information files. Any other relevant data are available from the corresponding authors upon request.

Code availability

The algorithms applied in this work can be built following the instructions in Methods and Supplementary Information. The codes that support the findings of this study are also available from the corresponding authors on request.

References

- Chen, Y. et al. Multidimensional nanoscopic chiroptics. *Nat. Rev. Phys.* **4**, 113–124 (2021).
- Tang, Y. & Cohen, A. E. Optical chirality and its interaction with matter. *Phys. Rev. Lett.* **104**, 163901 (2010).
- Zhang, Z. et al. Recent advances in reconfigurable metasurfaces: principle and applications. *Nanomaterials* **13**, 534 (2023).
- Yoo, S. & Park, Q. Metamaterials and chiral sensing: a review of fundamentals and applications. *Nanophotonics* **8**, 249–261 (2019).
- Han, Y. et al. Reprogrammable optical metasurfaces by electro-mechanical reconfiguration. *Opt. Express* **29**, 30751–30760 (2021).
- Li, K. et al. Electrically switchable, polarization-sensitive encryption based on aluminum nanoaperture arrays integrated with polymer-dispersed liquid crystals. *Nano Lett.* **21**, 7183–7190 (2021).
- Li, J. & Liu, Z. Focused-ion-beam-based nano-kirigami: from art to photonics. *Nanophotonics* **7**, 1637–1650 (2018).

8. Liu, Z. et al. Nano-kirigami with giant optical chirality. *Sci. Adv.* **4**, eaat4436 (2018).
9. Liu, Z. et al. Fano-enhanced circular dichroism in deformable stereo metasurfaces. *Adv. Mater.* **32**, 1907077 (2020).
10. Tang, Y. et al. Nano-kirigami metasurface with giant nonlinear optical circular dichroism. *Laser Photon. Rev.* **14**, 2000085 (2020).
11. Li, X. et al. Phase enabled circular dichroism reversal in twisted bi-chiral propeller metamolecule arrays. *Adv. Opt. Mater.* **9**, 2101191 (2021).
12. Liu, X. et al. Broadband and high-efficiency polarization conversion with a nano-kirigami based metasurface. *Sci. Rep.* **13**, 7454 (2023).
13. Chen, S. et al. Electromechanically reconfigurable optical nano-kirigami. *Nat. Commun.* **12**, 1299 (2021).
14. Zhao, Y. et al. Thermally actuated micro-/nanoscale deformations for optical reconfigurations. *J. Opt.* **24**, 054007 (2022).
15. Hu, Y. et al. Electrically tunable multifunctional polarization-dependent metasurfaces integrated with liquid crystals in the visible region. *Nano Lett.* **21**, 4554–4562 (2021).
16. Ji, Y. et al. Active terahertz spin state and optical chirality in liquid crystal chiral metasurface. *Phys. Rev. Mater.* **5**, 085201 (2021).
17. Jiang, X. et al. Terahertz polarization and chirality modulation induced by asymmetry inversion combining chiral metasurface and liquid crystal anisotropy. *Opt. Lett.* **48**, 1682–1685 (2023).
18. Bisoyi, H. K. & Li, Q. Liquid crystals: versatile self-organized smart soft materials. *Chem. Rev.* **122**, 4887–4926 (2022).
19. Luo, Z., Li, Y., Semmen, J., Rao, Y. & Wu, S. Achromatic diffractive liquid-crystal optics for virtual reality displays. *Light-Sci. Appl.* **12**, 230 (2023).
20. Cho, S., Yoshida, H. & Ozaki, M. Emission direction-tunable liquid crystal laser. *Adv. Opt. Mater.* **8**, 2000375 (2020).
21. Huang, M. et al. Dynamically tunable structural colors enabled by pixelated programming of soft materials on thickness. *Adv. Opt. Mater.* **11**, 2300573 (2023).
22. Kim, I. et al. Stimuli-responsive dynamic metaholographic displays with designer liquid crystal modulators. *Adv. Mater.* **32**, e2004664 (2020).
23. Sharma, M., Hendler, N. & Ellenbogen, T. Electrically switchable color tags based on active liquid-crystal plasmonic metasurface platform. *Adv. Opt. Mater.* **8**, 1901182 (2020).
24. Shen, Z. et al. Liquid crystal integrated metalens with tunable chromatic aberration. *Adv. Photonics* **2**, 036002 (2020).
25. Zhou, S. et al. Liquid crystal integrated metalens with dynamic focusing property. *Opt. Lett.* **45**, 4324–4327 (2020).
26. Tzeng, S. Y., Chen, C. & Tzeng, Y. Thermal tuning band gap in cholesteric liquid crystals. *Liq. Cryst.* **37**, 1221–1224 (2010).
27. Chen, P. et al. Chirality invertible superstructure mediated active planar optics. *Nat. Commun.* **10**, 2518 (2019).
28. Nys, I., Berteloot, B. & Neyts, K. Photoaligned chiral liquid crystal grating with hysteresis switching. *Adv. Opt. Mater.* **10**, 2201289 (2022).
29. Li, S. L. et al. Geometric phase-encoded stimuli-responsive cholesteric liquid crystals for visualizing real-time remote monitoring: humidity sensing as a proof of concept. *Light-Sci. Appl.* **13**, 27 (2024).
30. Chen, P., Wei, B. Y., Hu, W. & Lu, Y. Q. Liquid-crystal-mediated geometric phase: from transmissive to broadband reflective planar optics. *Adv. Mater.* **32**, e1903665 (2020).
31. Zhang, Y. H. et al. Logical rotation of non-separable states via uniformly self-assembled chiral superstructures. *Nat. Commun.* **15**, 1108 (2024).
32. de Gennes, P. G. & Prost, J. *The Physics of Liquid Crystals* 2nd edn, Vol. 614 (Oxford University Press, 1993).
33. Liu, Z., Du, H., Li, Z. Y., Fang, N. X. & Li, J. Nano-kirigami metasurfaces by focused-ion-beam induced close-loop transformation. *APL Photonics* **3**, 100803 (2018).
34. Han, Y. et al. Cascaded multilayer nano-kirigami for extensible 3D nanofabrication and visible light manipulation. *Photonics Res.* **8**, 1506 (2020).
35. Ji, C. Y. et al. Artificial propeller chirality and counterintuitive reversal of circular dichroism in twisted meta-molecules. *Nano Lett.* **21**, 6828–6834 (2021).
36. Liu, X., Liang, Q., Zhang, X., Ji, C. Y. & Li, J. Nano-kirigami enabled chiral nano-cilia with enhanced circular dichroism at visible wavelengths. *Nanophotonics* **12**, 1459–1468 (2023).
37. Yoon, H. G., Dierking, I. & Gleeson, H. F. Cholesteric pitch divergence near smectic phase transitions. *Phys. Rev. E* **82**, 011705 (2010).
38. Chen, S. et al. Plasmonic diastereoisomer arrays with reversed circular dichroism simply controlled by deformation height. *APL Photonics* **7**, 056102 (2022).
39. Zhang, Y. H. et al. Dynamically selective and simultaneous detection of spin and orbital angular momenta of light with thermo-responsive self-assembled chiral superstructures. *ACS Photonics* **9**, 1050–1057 (2022).
40. Zheng, X. et al. Highly efficient and ultra-broadband graphene oxide ultrathin lenses with three-dimensional subwavelength focusing. *Nat. Commun.* **6**, 8433 (2015).
41. Cao, G., Gan, X., Lin, H. & Jia, B. An accurate design of graphene oxide ultrathin flat lens based on Rayleigh-Sommerfeld theory. *Opto Electron. Adv.* **1**, 18001201–18001207 (2018).
42. Lin, H. et al. Diffraction-limited imaging with monolayer 2D material-based ultrathin flat lenses. *Light Sci. Appl.* **9**, 137 (2020).
43. Pahlevaninezhad, H. et al. Nano-optic endoscope for high-resolution optical coherence tomography in vivo. *Nat. Photonics* **12**, 540–547 (2018).
44. Ren, H. et al. An achromatic metafiber for focusing and imaging across the entire telecommunication range. *Nat. Commun.* **13**, 4183 (2022).
45. Sha, X. et al. Chirality tuning and reversing with resonant phase-change metasurfaces. *Sci. Adv.* **10**, eadn9017 (2024).
46. Chen, T. L. et al. A 2D chiral microcavity based on apparent circular dichroism. *Nat. Commun.* **15**, 3072 (2024).

Acknowledgements

S.F.L. and Y.H.Z. contributed equally to this work. This work is supported by the National Natural Science Foundation of China (Grant Nos. 52488301 (J.F.L.), T2325005 (J.F.L.), 62205022 (Y.W.), 62222507 (P.C.), 62375016 (J.F.L.), and 62175101 (P.C.)), the National Key Research and Development Program of China (Grant No. 2024YFB2809204 (J.F.L.)), the National Science Foundation of Jiangsu Province (Grant No. BK20243067 (Y.Q.L.)), Australia Research Council (Grant No. DP220100603 (B.H.J. and H.L.), FT210100806 (B.H.J.), FT220100559 (H.L.)) and Industrial Transformation Training Centre scheme (Grant No. IC180100005 (B.H.J. and H.L.)) and Linkage Project scheme (LP210200345 (B.H.J. and H.L.), LP210100467 (H. L.)), the Beijing Natural Science Foundation (No. Z2400005(Y.W.)), and the Beijing Institute of Technology Research Fund Program for Young Scholars. The authors thank the Analysis & Testing Center of Beijing Institute of Technology.

Author contributions

Y.W., P.C., and S.F.L. conceived the original idea. J.F.L., X.L., Q.H.L., H.Z.S. and Y.Y.Z. designed and fabricated the nano-cilia metasurface; Y.H.Z. and P.C. designed and fabricated the cholesteric LC samples; S.F.L. and Y.H.Z. conducted the numerical simulations on optical properties of the dual chiral framework; H.L., G.Y.C., and S.F.L. designed the CPL metalens; S.F.L. and X.C.Z. performed the experiments; S.F.L., Y.H.Z., Y.W., P.C., H.L., and Z.Y.W. analyzed the data; S.F.L. and Y.W. prepared the initial manuscript; J.F.L., Y.Q.L., and B.H.J. co-supervised and directed the research. All authors participated in the discussion, and contributed to refining the manuscript.

Competing interests

The authors declare no competing interest.

Additional information

Supplementary information The online version contains supplementary material available at <https://doi.org/10.1038/s41467-025-61982-w>.

Correspondence and requests for materials should be addressed to Yang Wang, Peng Chen, Han Lin or Jiafang Li.

Peer review information *Nature Communications* thanks X and the other anonymous reviewer(s) for their contribution to the peer review of this work. A peer review file is available.

Reprints and permissions information is available at <http://www.nature.com/reprints>

Publisher's note Springer Nature remains neutral with regard to jurisdictional claims in published maps and institutional affiliations.

Open Access This article is licensed under a Creative Commons Attribution-NonCommercial-NoDerivatives 4.0 International License, which permits any non-commercial use, sharing, distribution and reproduction in any medium or format, as long as you give appropriate credit to the original author(s) and the source, provide a link to the Creative Commons licence, and indicate if you modified the licensed material. You do not have permission under this licence to share adapted material derived from this article or parts of it. The images or other third party material in this article are included in the article's Creative Commons licence, unless indicated otherwise in a credit line to the material. If material is not included in the article's Creative Commons licence and your intended use is not permitted by statutory regulation or exceeds the permitted use, you will need to obtain permission directly from the copyright holder. To view a copy of this licence, visit <http://creativecommons.org/licenses/by-nc-nd/4.0/>.

© The Author(s) 2025